Lab on a Chip

Integrating Nanofibers with Biochemical Gradients to Investigate Physiologically-Relevant Fibroblast Chemotaxis

Journal:	*Lab on a Chip*
Manuscript ID	LC-ART-06-2019-000602.R1
Article Type:	Paper
Date Submitted by the Author:	21-Aug-2019
Complete List of Authors:	Morrow, Carmen; Virginia Polytechnic Institute and State University Mukherjee, Apratim; Virginia Polytechnic Institute and State University Traore, Mahama; Virginia Polytechnic Institute and State University Leaman, Eric; Virginia Polytechnic Institute and State University Kim, AhRam; Virginia Polytechnic Institute and State University Smith, Evan; Virginia Polytechnic Institute and State University Nain, Amrinder; Virginia Polytechnic Institute and State University Behkam, Bahareh; Virginia Polytechnic Institute and State University

ARTICLE

Integrating Nanofibers with Biochemical Gradients to Investigate Physiologically-Relevant Fibroblast Chemotaxis

Received 00th January 20xx,
Accepted 00th January 20xx

DOI: 10.1039/x0xx00000x

Carmen M. Morrow[a], Apratim Mukherjee[a], Mahama A. Traore[a,b], Eric J. Leaman[a], AhRam Kim[a], Evan M. Smith[a], Amrinder S. Nain[a,b], Bahareh Behkam[a,b,*]

Persistent cell migration can occur due to anisotropy in the extracellular matrix (ECM), the gradient of a chemo-effector, or a combination of both. Through a variety of *in vitro* platforms, the contributions of either stimulus have been extensively studied, while the combined effect of both cues remains poorly described. Here, we report an integrative microfluidic chemotaxis assay device that enables the study of single cell chemotaxis on ECM-mimicking, aligned, and suspended nanofibers. Using this assay, we evaluated the effect of fiber spacing on the morphology and chemotaxis response of embryonic murine NIH/3T3 fibroblasts in the presence of temporally invariant, linear gradients of platelet-derived growth factor-BB (PDGF-BB). We found that the strength of PDGF-mediated chemotaxis response depends on not only the gradient slope but also the cell morphology. Low aspect ratio (3.4±0.2) cells on flat substrata exhibited chemotaxis response only at a PDGF-BB gradient of 0-10 ng/mL. However, high aspect ratio (19.1±0.7) spindle-shaped cells attached to individual fibers exhibited maximal chemotaxis response at a ten-fold shallower gradient of 0-1 ng/mL, which was robustly maintained up to 0-10 ng/mL. Quadrilateral-shaped cells of intermediate aspect ratio (13.6±0.8) attached to two fibers exhibited a weaker response compared to the spindle-shaped cells, but still stronger compared to cells attached to 2D featureless substrata. Through pharmacological inhibition, we show that the mesenchymal chemotaxis pathway is conserved in cells on fibers. Altogether, our findings show that chemotaxis on ECM-mimicking fibers is modulated by fiber spacing-driven cell shape and can be significantly different from the behavior observed on flat 2D substrata. We envisage that this microfluidic platform will have wide applicability in understanding the combined role of ECM architecture and chemotaxis in physiological and pathological processes.

Introduction

Physiological and pathological processes including embryogenesis[1], wound healing[2,3], and cancer metastasis[4] are driven by chemotaxis (*i.e.,* directed migration in response to the spatial gradient of a soluble chemo-effector) and guided by the fibrous network of the extracellular matrix (ECM). In wound healing, platelet granules and inflammatory cells at the wound site release several growth factors including the platelet-derived growth factor-BB (PDGF-BB), which plays an important role in the recruitment and activation of the local fibroblasts[2]. In cancer progression, growth factors such as PDGF-BB and transforming growth factor-β (TGF-β) secreted by cancer cells play a crucial role in the recruitment of cancer-associated fibroblasts (CAFs) through chemotactic response. Studies have shown that CAFs are important to both initial tumor development and cancer cell invasive behavior as they constantly remodel and organize the ECM in the vicinity of the tumor, which is believed to promote cancer invasion into surrounding tissue and metastasis[5–8].

Chemotaxis has long been observed and studied in eukaryotic cells using classical methods such as capillary assay[9], Boyden chamber[10], or Zigmond chamber[11]. While these assays have been vital in understanding the fundamentals of chemotaxis and overall cell migration, they are unable (i) to establish gradients that are both measurable and stable over long periods of time[9–13], a requisite for studying slow-moving cells; and (ii) to recapitulate the three-dimensional (3D) and anisotropic arrangement of the fibrous ECM[14–17]. The advent of microfluidics has substantially enhanced the generation of stable chemo-effector gradients through diffusion-based mixing (for recent reviews, see refs.[18,19]); nevertheless, chemotaxis studies in microfluidic devices have rarely focused on the role of ECM-mimicking topography on chemotaxis response. It is now well-recognized that substratum topography has a profound effect on cell migratory behavior and phenotype[20,21]. As such, many recent cell migration studies are conducted on physiologically relevant topography that replicates one or more aspects of the ECM that cells migrate upon *in vivo*[20,22–31]. The majority of these studies utilize 3D gels made of either ECM proteins such as collagen and fibrin or non-biological hydrogels[23,27–31]. However, high-resolution imaging and tracking of individual cells, which is important for understanding cell migration on a fundamental level, is a well-known challenge in 3D gel studies[32,33]. Furthermore, heterogeneity in gel physical properties (e.g., the diameter of fibrils, crosslinking density) is an added complexity. In order to mitigate the challenges of studying 3D migration while still capturing the effects of physiologically relevant topographical features, a few studies by us and others have used single and multi-fiber-based reductionist approaches, which enable the study of cell behavior in response to well-defined and highly repeatable biophysical cues[20,26,34–38]. However, little is known about the chemotactic behavior of cells on suspended fibers mimicking the native ECM.

---

[a] *Department of Mechanical Engineering, Virginia Tech, Blacksburg, VA 24061, USA.*
[b] *School of Biomedical Engineering & Sciences, Virginia Tech, Blacksburg, VA 24061, USA.*
** Corresponding author. Email: behkam@vt.edu*

Electronic Supplementary Information (ESI) available: See DOI: 10.1039/x0xx00000x

Here, we present a flow-based microfluidic assay that combines a time-invariant and quantifiable chemical gradient with suspended aligned nanofibers of uniform diameter and controlled spacing. Using this assay, we investigated the effect of fiber spacing on fibroblast morphology and migratory behavior and quantitated its chemotaxis response in the presence of linear gradients of PDGF-BB, a well-known chemoattractant and mitogen for fibroblasts[39,40]. We show that the chemotaxis response varies with cell shape (modulated by the inter-fiber spacing) and that cells with higher aspect ratio are more sensitive to PDGF-BB gradients. Notably, we demonstrate cells attached to individual fibers in elongated shapes are remarkably more sensitive to PDGF-BB and chemotactically respond to an order of magnitude shallower PDGF-BB gradients compared to the cells on flat substrata. Through pharmacological treatment, we show that mesenchymal chemotaxis pathway is conserved in cells on fibers. Development of microfluidic assays that combine stable and quantifiable chemical gradients with ECM-mimicking suspended fibers provide new contextual tools to interrogate the cell decision-making process in a controlled and repeatable manner.

Experimental

Fabrication of the Suspended Nanofiber Array

Biocompatible 316 stainless steel (Motion Industries, Roanoke, VA) was cut into 2 mm × 5 mm scaffolds with a 1.7 mm × 1.7 mm square opening. Polystyrene nanofibers were deposited on the stainless steel scaffold using the non-electrospinning Spinneret based Tunable Engineered Parameters (STEP) method[41–43]. Briefly, polystyrene (PS, Scientific Polymer Products, Ontario, NY, M_w: 2 x 10^6 g mol^{-1}) was dissolved in p-xylene (Fischer Scientific, Pittsburgh, PA) at 14% (w/w) and the solution was extruded through a needle to deposit suspended and highly aligned fibers at precise spacing of 15 µm or 25 µm. The nanofiber arrays were exposed to the vapor phase of tetrahydrofuran (a polystyrene good solvent) to fuse them to the surface of the stainless steel scaffold and create fixed-fixed boundary conditions at the ends of the suspended fibers (**Figure S1**). The diameter of the fibers was 535 ± 9 nm (n=120), as determined by scanning electron microscopy (SEM). This fiber diameter falls within the range of *in vivo* ECM fiber diameters which are as small as 50 nm (collagen fibrils) and as large as a few micrometers (collagen fibers)[44,45]. Furthermore, polystyrene and collagen have similar Young's moduli of ~1-3 GPa[46,47]. The ECM porosity varies widely from > 100 µm^2 in loose connective tissue and lymph nodes to < 1 µm^2 in dense collagen bundles[48]. Thus, the ranges of fiber spacing chosen by us fall within the *in vivo* range and result in physiologically relevant cell shapes[49,50].

Fabrication of the Microfluidic Device

The diffusive mixer design was inspired by the pioneering work of N. Jeon *et al.*[51] and was microfabricated from polydimethylsiloxane (PDMS) using standard soft lithography techniques[52]. A schematic of the microfluidic platform is shown in **Figure 1a**. The PDMS device has two inlets, one for a buffer solution and the other for the chemo-effector of interest, which feed into the network of diffusive mixing channels. Prior to irreversible bonding of the PDMS to the glass slide, two arrays of suspended nanofibers were adhered onto the glass slide with medical-grade epoxy (Master Bond, Hackensack, NJ). The nanofiber arrays were placed in series in the observation channel with fibers aligned with the direction of the chemical gradient and perpendicular to the flow direction (**Figure 1a**). The inlet flow rates and the diffusive mixer pattern were carefully designed in order to establish a linear chemical gradient over the length of the fibers (see ESI document for microfluidic device design detail). Eleven channels exit from the serpentine diffusive mixing channels and converge into an observation channel 2.2 mm × 15 mm, developing a linear chemical gradient downstream. All channels were 500 µm in height in order to minimize shear forces on cells migrating on the suspended nanofibers deposited on the 75 µm thick stainless steel scaffolds. The negligible effect of the shear force on cell migratory behavior was confirmed by the lack of a statistically significant difference in migration speed of the cells on similar nanofiber scaffolds in the microfluidic device and in well plates (**Figure S2**).

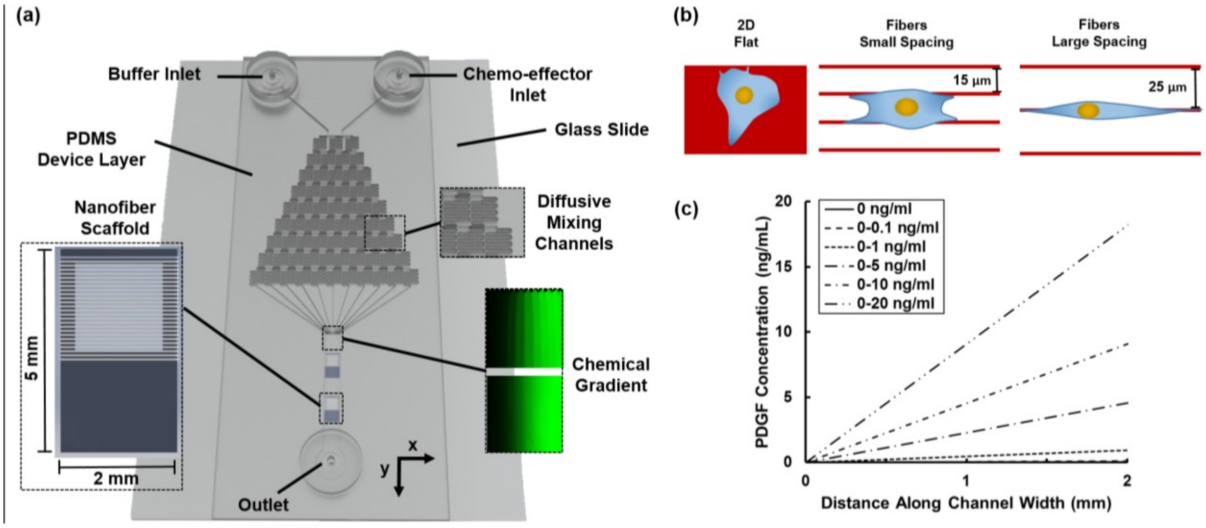

Fig. 1 Microfluidic assay device for characterizing chemotaxis response on ECM-mimicking suspended nanofibers. (a) Schematic of the microfluidic assay device with ECM-mimicking suspended fiber arrays placed in the observation channel. The fluorescence inset images show the fluorescein (surrogate for PDGF-BB) gradient generated at the entrance to the observation channel and downstream near the nanofiber scaffold. (b) The schematics show the three different substratum types tested—2D flat polystyrene, 500 nm diameter polystyrene fibers at 15 µm spacing, and 500 nm diameter polystyrene fibers at 25 µm spacing, resulting in spread, quadrilateral, and spindle morphologies, respectively. (c) 3T3 cells were subjected to linear PDGF-BB gradients of 0-0.1, 0-1, 0-5, 0-10, 0-20 ng/mL across the 2.2 mm width of the observation channel. The repeated splitting and mixing of the flow in the diffusive mixing channels ensures a steady linear concentration gradient along the suspended fibers.

Cell Culture

NIH/3T3 fibroblasts (ATCC CRL-1658, American Type Culture Collection, Manassas, VA) were cultured in Dulbecco's Modified Eagle Medium (DMEM, American Type Culture Collection, Manassas, VA) supplemented with 10% (v/v) calf bovine serum (CBS, American Type Culture Collection, Manassas, VA) and were maintained at 37 ˚C and 5% CO_2. To circumvent the need for CO_2 during experimentation, the cells were adapted to a CO_2-independent medium (Thermo Fisher Scientific, Waltham, MA) supplemented with 10% (v/v) CBS and 2% (v/v) 200 mM L-glutamine (Fisher Scientific, Pittsburgh, PA) for 24 hours prior to each experiment. The culture density was approximately 5×10^4 cells/cm^2 at the start of media adaptation. The CO_2-independent medium culture was stored in a 37 °C humid incubator.

Migration and Chemotaxis Assay in the Microfluidic Device

The assembled microfluidic device was first primed with 100% ethanol and then filled with autoclaved deionized (DI) water. Fibronectin at a concentration of 5 µg/mL (Sigma-Aldrich, St. Louis, MO) in phosphate-buffered saline (PBS) was flowed through the device at 20 µL/min for 5 min to replace the PBS. The flow was then stopped, and the device was incubated at 37 °C for 3 hours to facilitate uniform fibronectin coating of the substrata (i.e., polystyrene nanofibers or flat polystyrene substrata (control), **Figure 1b**). After incubation, CO_2-independent medium supplemented with 10% (v/v) CBS, 2% (v/v) 200 mM L-glutamine, and 1% (v/v) penicillin-streptomycin (Fisher Scientific, Pittsburgh, PA) was flowed through the device at 20 µL/min for a minimum of 5 min. A syringe containing ~ 10^5 cells/mL was inserted into the outlet tube, and the suspension was manually pushed into the device. The device was left at 37 °C for 3 hours to allow cell attachment to the substratum. After attachment, one of the CO_2-independent medium inlet syringes was exchanged for a syringe containing the selected PDGF-BB (Fisher Scientific, Pittsburgh, PA) concentration in CO_2-independent medium (**Figure 1c**). The PDGF-BB and CO_2-independent medium were flowed at a combined flowrate of 1 µL/min (500 nL/min per syringe) for 2 hours to establish a linear PDGF-BB gradient throughout the length of the observation channel. This flowrate was maintained throughout the duration of the experiment. Cells remained viable and motile for the entire 12-hour duration of the experiment. Cell behavior was analyzed during the final 6 hours, wherein no measurable influence on cell motile behavior was measured (**Figure S3**). A Zeiss AxioObserver.Z1 inverted microscope equipped with an AxioCam MRm camera and a 20× objective was used to capture images of cells every 10 min. Zen software (Zeiss Microscopy, Oberkochen, Germany) was used to create tiled images of the entire nanofiber length.

Blebbistatin Experiments

Pharmacological studies were performed to determine the role of mesenchymal chemotaxis pathway in chemotaxis response of fibroblast cells on suspended nanofibers. Chemotaxis assays were conducted in the presence of Myosin II inhibitor – Blebbistatin (BLB; Enzo Life Sciences, Farmingdale, NY). For these experiments, a 10 mM stock solution of BLB was first prepared in dimethyl sulfoxide (DMSO; American Type Culture Collection, Manassas, VA). Subsequently, after the stable attachment of the cells to the substrata, as described above, BLB was introduced into the device via both the inlet syringes at a concentration of 15 µM and the device was incubated for 2 hours prior to imaging. After the 12 hour imaging period, the BLB was washed out from the device by reintroduction of CO_2-independent medium in one syringe and PDGF-BB in CO_2-independent medium through the other syringe, thus re-establishing the PDGF-BB gradient in the absence of BLB. The cells were imaged for 6 additional hours to confirm that the BLB effect was reversible.

Data Analysis

All reported results are obtained from at least three independent experiments for each PDGF-BB gradient, substratum type, and pharmacological treatment. All microscopy images were processed and exported to ImageJ (NIH, Bethesda, MD) for analysis. Any cells that interacted with other cells, interacted with the substratum edge, divided, or died during the experiment, were excluded. A displacement criterion of 10 µm/h for at least half of the experiment duration was used to omit non-migratory cells from the analysis. All data are expressed as means±S.E. All statistical analyses were performed in OriginPro (OriginLab, Northampton, MA). A two-sample *t*-test was performed on data with two categories. Data with more than two categories were analyzed using the one-way analysis of standard variance (ANOVA) method followed by Fisher's Least Significant Difference (LSD) test. Differences between results were considered statistically significant when the *p*-value was less than 0.05.

Results and discussion

Effect of fiber spacing on NIH/3T3 fibroblast shape and migratory behavior

NIH/3T3 fibroblast morphology and migratory behavior were studied in the microfluidic assay device on suspended, aligned, polystyrene nanofibers with either 15 µm (small) or 25 µm (large) spacing, and on flat polystyrene substrata (control) in the absence of a PDGF-BB gradient. As shown in **Figures 1b** and **2a**, cell morphology was observed to be substratum dependent and is referred to as spread (on flat substratum), quadrilateral (on fibers with 15 µm spacing), and spindle (on fibers with 25 µm spacing). In both cases, cell movement is constrained to one-dimension (1D) along the length of the fibers. Cell shape on the three different substrata was quantitatively compared using the metric aspect ratio (AR), defined as

$$AR = \frac{l}{w} \tag{1}$$

where l is the cell length and w is the cell width, respectively. Both the length and the width were measured through the center of the cell nucleus. For consistency, the aspect ratio measurements for cells on flat substrata were only taken when the cell was aligned with the channel width, the same orientation as cells on fibers and the chemical gradients (in the chemotaxis experiments). As shown in **Figure 2b**, cells on flat polystyrene had the lowest aspect ratio (3.4±0.2) followed by cells on nanofibers with small spacing (13.6±0.8), and nanofibers with large spacing (19.1±0.7). The migratory behavior of the cells on the three substratum types was studied next. Cell positions were tracked every 10 minutes for 6 hours. Representative cell trajectories on each substratum type are shown in **Figure 2c (i-iii)**. On average, spindle-shaped cells displaced 3791±481 µm, whereas quadrilateral-shaped cells only displaced 1945±264 µm. Cells in spread morphology displaced the least with

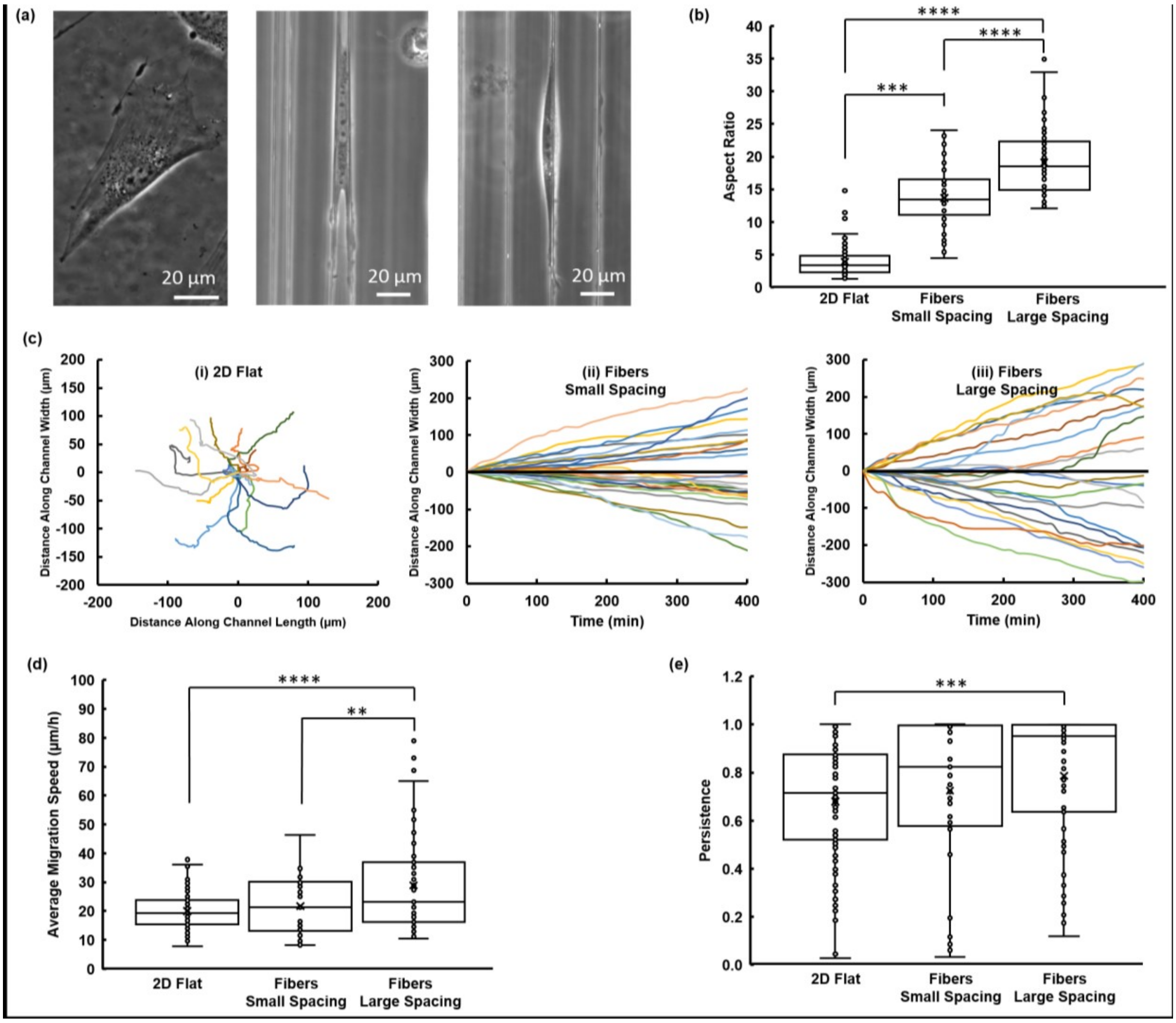

Fig. 2 Effect of fiber spacing on cell morphology and migratory behavior. (a) Phase-contrast optical microscopy images of the 3T3 cell morphology on flat substratum, suspended nanofibers with small spacing, and suspended nanofibers with large spacing (from left to right). Cells are in the well-recognized spread morphology on the flat substratum, whereas cells achieve "quadrilateral" shapes on fibers with small spacing and "spindle" shapes on the fibers with large spacing. (b) Cell aspect ratio on 2D flat polystyrene (n=111), fibers with small spacing (n=37), and fibers with large spacing (n=52). (c) Representative cell trajectories on each of the three substratum types. Because cell migration on fibers was limited to 1D, the trajectories were plotted as a function of time. Individual trajectories are represented in different colors. Initial positions of the cells were superimposed at the origin for comparison. The zero displacement reference line (black) delineates cells moving in positive and negative x-directions. Each plot depicts data from 20 cells. (d) Average cell migration speed on 2D flat polystyrene (n = 111), polystyrene fibers with small spacing (n = 37), and polystyrene fibers with large spacing (n = 67). (e) Persistence on 2D flat polystyrene (n = 111), polystyrene fibers with small spacing (n = 37), and polystyrene fibers with large spacing (n = 67). Error bars in (b), (d), and (e) represent 95% percentile of data. ***p* value <0.01, ****p* < 0.001, *****p* < 0.0001.

an average of 156±11 µm over the 6 hour duration. The migration speed and persistence of the cells were computed to quantitatively compare their migratory behavior on the three substrata. Average migration speed, V_{avg}, was defined as the average of instantaneous speed of the cell and was calculated according to

$$V_{\text{avg}} = \frac{\sum_{i=1}^{37}|\mathbf{r}_{i+1}-\mathbf{r}_i|}{t} \qquad (2)$$

Where $\mathbf{r}_i$ represents the cell location at the i^{th} time point, and t is the duration of the experiment (6 hours). As shown in **Figure 2d**, the average cell speed on the flat substratum was the lowest at 19.9±0.6 µm/hr. Cells on fibers with small spacing had a slightly higher average speed of 21.7±1.6 µm/hr, although no statistically significant difference between the two groups was observed. For cells on fibers with large spacing, the average speed of 28.8±2.1 µm/hr was 45% higher than the average speed of cells on flat polystyrene. These findings are consistent with prior works demonstrating a correlation between cell shape and migration speed, wherein cells in more elongated (polarized) morphology have higher migration speed[37,57]. To assess the directionality of cell migration on each substratum, persistence, defined as the ratio of the magnitude of the displacement vector to the total distance travelled by the cell, was quantitated next:

$$\text{Persistence} = \frac{|\mathbf{r}_{\text{final}}-\mathbf{r}_{\text{initial}}|}{\sum_{i=1}^{i=37}|\mathbf{r}_{i+1}-\mathbf{r}_i|} \qquad (3)$$

The average persistence was the lowest on the flat substratum at 0.68±0.02. Persistence of the cells on fibers with small spacing was only slightly higher with an average value of 0.73±0.05, whereas on fibers with large spacing the persistence was considerably higher at 0.83±0.03. This 22% increased persistence of cells migrating on suspended nanofibers with large spacing, compared to flat polystyrene, was statistically significant. However, no statistically significant difference was observed between the two nanofiber groups, suggesting that differences in fiber spacing-induced cell morphology do not affect the persistence of fibroblast cells (**Figure 2e**).

NIH/3T3 fibroblast migration in linear PDGF-BB gradients

Next, the effect of substratum type and the corresponding cell morphologies on the NIH/3T3 fibroblast cell chemotaxis response was investigated. Time-invariant linear PDGF-BB gradients with different slopes were established across the width of the observation channel, along the flat substrata or the 1.5 mm length of the suspended nanofibers, and chemotaxis response of cells in the three aforementioned morphologies was interrogated. Four concentration ranges of 0-1, 0-5, 0-10, and 0-20 ng/mL (corresponding to gradients of 0.45, 2.3, 4.5, and 9 ng/mL/mm, respectively, **Figure 1c**) were tested. The range of PDGF-BB concentrations utilized in this work is in line with reported values for *in vivo* PDGF concentrations[53–56]. Cell positions were tracked every 10 minutes for 6 hours. Representative migration trajectories of the cells on each substratum type in the presence of 0-1 ng/mL and 0-10 ng/mL of PDGF-BB are shown in **Figure 3a**. Compared to **Figure 2c**, the trajectories in **Figure 3a**

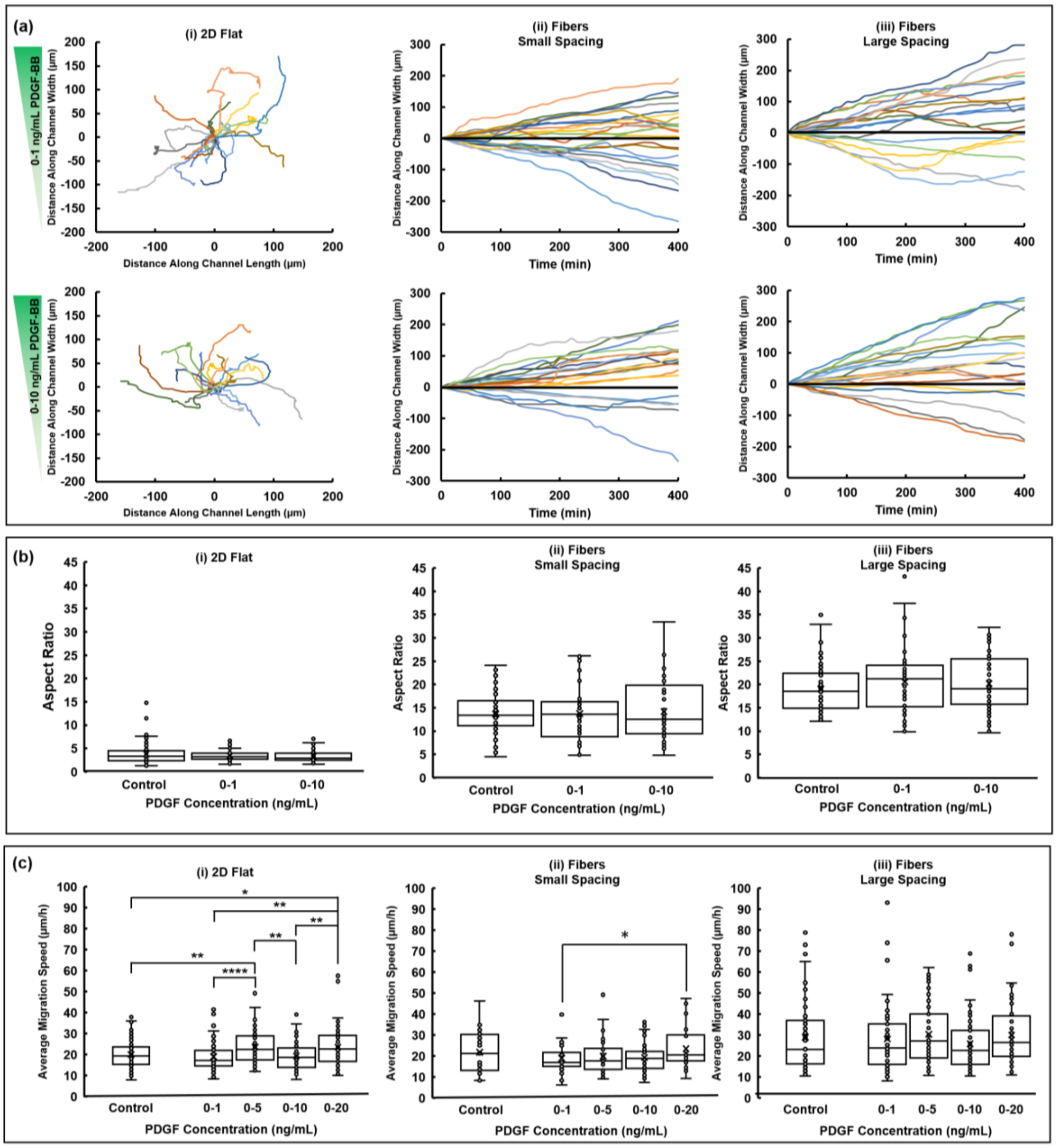

Fig. 3 Effect of fiber spacing on cell morphology and migratory behavior in presence of PDGF-BB gradients. (a) Representative cell migration trajectories on each of the three substratum types in presence of 0-1 ng/mL and 0-10 ng/mL PDGF-BB concentration gradients. Individual trajectories are represented in different colors. Initial positions of the cells were superimposed at the origin for comparison. The zero displacement reference line (black) delineates cells moving up (positive) and down (negative) the chemoattractant gradient. Each plot depicts data from 20 cells. (b) Cell aspect ratio on 2D flat polystyrene (n = 111, 56, and 53 for 0, 0-1, and 0-10 ng/ml PDGF-BB, respectively), fibers with small spacing (n = 37, 37, and 45 for 0, 0-1, and 0-10 ng/ml PDGF-BB, respectively), and fibers with large spacing (n = 52, 53, and 55 for 0, 0-1, and 0-10 ng/ml PDGF-BB, respectively). (c) Average cell migration speed on the 2D flat polystyrene, polystyrene fibers with small spacing, and polystyrene fibers with large spacing. The number of cells analyzed are 111, 56, 66, 54, and 53 on flat, 37, 37, 53, 45, and 25 on fibers with small spacing, and 67, 53, 59, 55, and 56 on fibers with large spacing, for 0, 0-1, 0-5, 0-10, and 0-20 ng/mL PDGF-BB, respectively. Error bars in (b) and (c) represent 95% percentile of data. **p* value <0.05, ***p* <0.01, *****p* < 0.0001.

showed biased movement on all the three substratum types. On flat substrata, trajectories in **Figure 2c-i** are randomly distributed whereas a clear bias (towards positive y-values) in trajectory distribution is observed in plots shown in **Figure 3a-i**, particularly in the presence of 0-10 ng/mL of PDGF-BB. Likewise, a larger number of the cells on fibers exhibited biased migration in the presence of the PDGF-BB gradients, as shown in **Figures 3a-ii** and **3a-iii,** compared with control (**Figures 2c-ii** and **2c-iii**).

The effect of gradient on aspect ratio and migration speed on each substratum type was investigated next. We found that the aspect ratio of the cells was independent of the gradients on all three substratum types (**Figure 3b**). Similarly, cell migration speed on fibers was found to be largely independent of the gradient irrespective of the fiber spacing (**Figures 3cii-3ciii**). In contrast, the migration speed of the cells on 2D flat substratum was sensitive to the gradient, as shown in **Figure 3ci**.

Next, three metrics of *Directional Persistence* (DP), Chemotaxis Index (CI), and *Population-Scale Chemotaxis Response* (CR) were identified to quantitatively compare the cells chemotactic behavior, at the single-cell and population-scale, as a function of the PDGF-BB gradient slope and the substratum type. DP was defined as the displacement vector divided by the total distance traveled (**Figure 4a**):

$$DP = \frac{\mathbf{r}_{\text{final}} - \mathbf{r}_{\text{initial}}}{\sum_{i=1}^{i=37} |\mathbf{r}_{i+1} - \mathbf{r}_i|} \qquad (3)$$

where $\mathbf{r}_{\text{final}}$ is the final cell position, $\mathbf{r}_{\text{initial}}$ is the initial cell position, and the denominator represents the total distance traveled by the cell over the duration of the experiment (**Figure 4a**). Physically, the DP value represents bias in cell migration towards the chemoattractant source, and its value ranges between -1 to 1. A DP value close to 1 indicates that the cell consistently migrated *towards* the source of the chemoattractant while a large negative DP value indicates that the cell predominantly migrated *away* from the chemoattractant source. As shown in **Figures 4b-c**, on flat substrata and on fibers with small spacing, only cells subjected to 0-10 ng/mL PDGF-BB gradient showed statistically significant higher DP values, compared to the control. In contrast, on the fibers with large spacing, the DP values at gradients of 0-1, 0-5, and 0-10 ng/mL were strikingly similar (0.31 ± 0.11, 0.31 ± 0.10, 0.32 ± 0.11, respectively) and significantly higher than that of the control (-0.005± 0.103) and the 0-20 ng/mL case (0.14± 0.12).

The chemotaxis response was further interrogated by evaluating the chemotaxis index (CI) on each substratum as a function of PDGF-BB gradient. CI was defined as

$$CI = \cos(\theta) = \left(\frac{|\Delta x|}{\Delta x}\right)\left[\cos\left(\tan^{-1}\left(\frac{|\Delta y|}{|\Delta x|}\right)\right)\right], \qquad (4)$$

where θ is the angle between the displacement vector and its component in the chemical gradient direction (**Figure 5a**), Δx and Δy are the cell displacement vector components parallel and perpendicular to the gradient, respectively. All displacement vectors were measured with respect to the initial and final cell positions. CI represents the strength of response to a chemoattractant gradient. A positive CI indicated the cell displaced towards the chemoattractant while a negative chemotactic index indicated the opposite. In comparison with DP, the trends in CI represent a finer

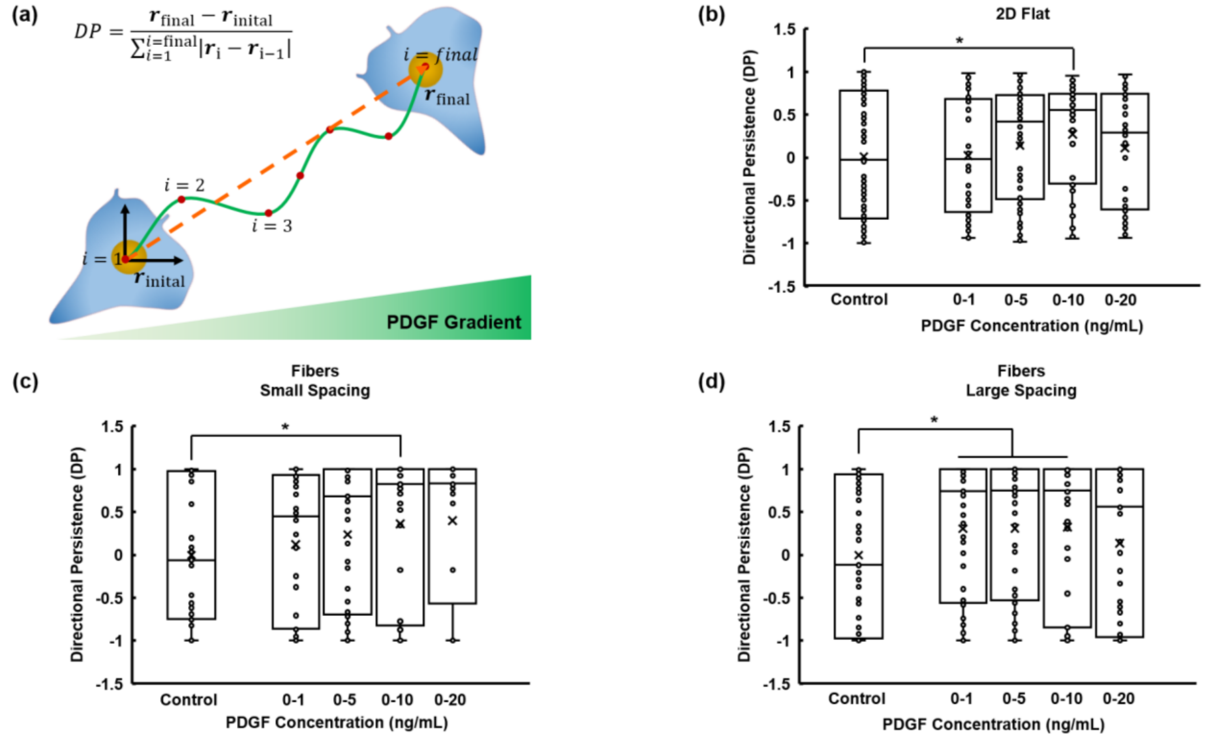

Fig. 4 Effect of fiber spacing on cell persistence in presence of PDGF-BB gradients. (a) Schematic showing the definition of the directional persistence (DP) parameter which signifies the bias in migration of the cell towards (positive) or away (negative) from the chemoattractant source. (b-d) The directional persistence values as a function of PDGF-BB concentration gradient for cells migrating on 2D flat polystyrene (b), polystyrene fibers with small spacing (c), and polystyrene fibers with large spacing (d). The black crosses represent the average values. The number of cells analyzed are 111, 56, 66, 54, and 53 on flat, 37, 37, 53, 45, and 25 on fibers with small spacing, and 67, 53, 59, 55, and 56 on fibers with large spacing, and for 0, 0-1, 0-5, 0-10, and 0-20 ng/mL PDGF-BB, respectively. Error bars in (b) - (d) represent 95% percentile of data. *p value <0.05.

delineation of the chemotactic response on the flat substratum as the angle θ can vary between 0° and 360° (**Figure 5b-i**). For the cells on fiber, due to the constraint of the migration path along the fiber, the CI will have either a value of 1 or -1. Thus, not surprisingly, the CI for cells on fibers followed the same trend as the DP with statistically significant differences in CI values between control (-0.03±1.01) and 0-10 ng/mL (0.42±0.92) on fibers with small spacing (**Figure 5b-ii**), and between control (-0.02±1.01) and 0-1, 0-5, and 0-10 ng/mL (0.36±0.94, 0.32±0.95, and 0.42±0.92) on fibers with large spacing (**Figure 5b-iii**).

We then defined a new metric, *Population-Scale Chemotaxis Response* (CR), which represents the percentage of cells with a positive CI for each PDGF-BB gradient and substratum type combination (**Figure 5c**). A CR value of 50% indicates that there was no bias in the population migration, while a CR value of 100% indicates that all cells displaced towards the chemo-attractant source. On the flat substratum, the CR gradually increased with an increase in the PDGF-BB gradient slope up to a maximum value of 70% ± 3.1% at a PDGF-BB concentration of 0-10 ng/mL. At a larger concentration of 0-20 ng/mL, response decreased to 58%± 0.2% and remained low even at the higher concentration of 0-100 ng/mL (data not shown), presumably due to the saturation of the chemoattractant receptors. Presence of a maximum CR value and saturation at higher gradients is well-expected for cell response to a chemoattractant, including PDGF-BB[40,58]. On fibers with large spacing (spindle-shaped cells), the maximum CR value of 71% ± 1.7% was observed at the concentration gradient of 0-10 ng/mL and a drop in chemotactic response at 0-20 ng/mL was observed, similar to cells migrating on flat polystyrene. However, a strikingly different behavior was observed at the intermediate gradient values, wherein strong chemotaxis responses were observed at significantly shallower PDGF-BB gradients of 0-1 (68% ± 0.5%) and 0-5 ng/mL (66% ± 2.6%). We did not observe a chemotaxis response (i.e., $CR \gg 50\%$) at the lower concentration gradient of 0-0.1 ng/mL (data not shown). Cells on fibers with small spacing (quadrilateral-shaped cells) responded to shallower PDGF-BB gradients as well. However, the CR values of 59% ± 4.9% and 60% ± 0.8% at the intermediate gradients of 0-1 and 0-5 ng/mL were weaker than the response of the cells on fibers with large spacing. At the optimal concentration gradient of 0-10 ng/mL, the CR value remained consistent with the other two substratum types at 71% ± 0.4% and a drop in chemotaxis response at 0-20 ng/mL was still observed. Altogether, we found that an equally strong chemotaxis response at the optimal chemoattractant gradient is observed irrespective of the substratum type. However, at less than optimal gradient, the response varied significantly with

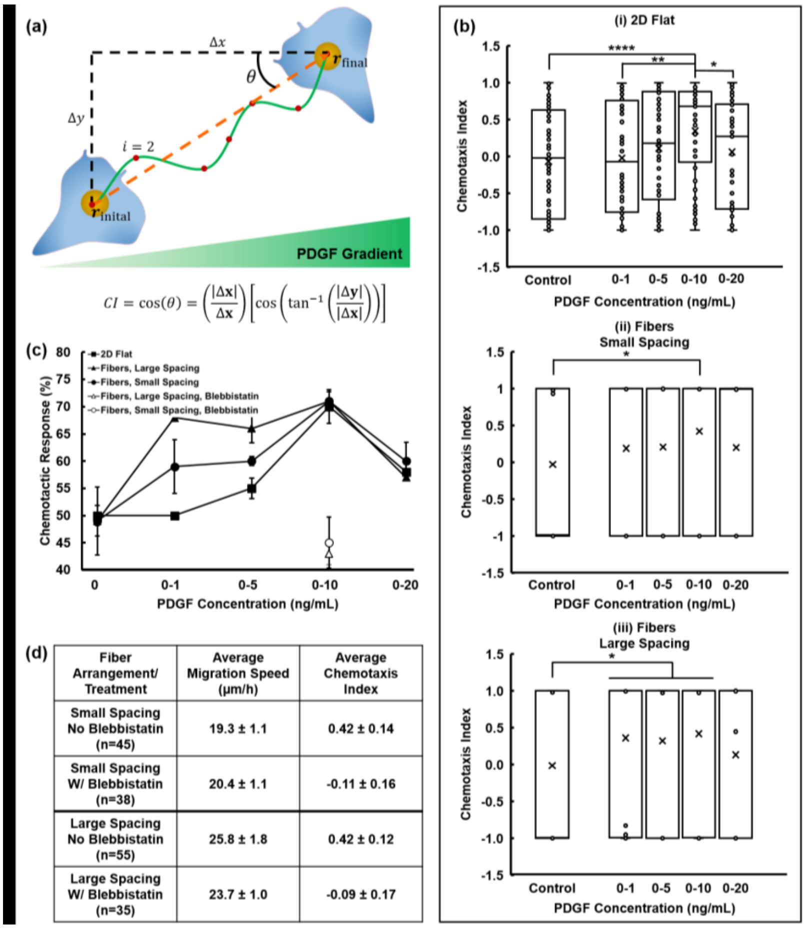

Fiber Arrangement/ Treatment	Average Migration Speed (μm/h)	Average Chemotaxis Index
Small Spacing No Blebbistatin (n=45)	19.3 ± 1.1	0.42 ± 0.14
Small Spacing W/ Blebbistatin (n=38)	20.4 ± 1.1	-0.11 ± 0.16
Large Spacing No Blebbistatin (n=55)	25.8 ± 1.8	0.42 ± 0.12
Large Spacing W/ Blebbistatin (n=35)	23.7 ± 1.0	-0.09 ± 0.17

Fig. 5 Effect of fiber spacing on single-cell and population-scale chemotaxis response in presence of PDGF-BB gradients. (a) Schematic showing the definition of the chemotaxis index (CI). (b) CI values as a function of PDGF-BB concentration gradient for cells migrating on 2D flat polystyrene, polystyrene fibers with large spacing, and polystyrene fibers with small spacing. The black crosses represent the average values. Error bars represent 95% percentile of data. The number of cells analyzed are 111, 56, 66, 54, and 53 on flat, 37, 37, 53, 45, and 25 on fibers with small spacing, and 67, 53, 59, 55, and 56 on fibers with large spacing for 0, 0-1, 0-5, 0-10, and 0-20 ng/mL PDGF-BB, respectively. *p value <0.05. (c) Chemotaxis response (*i.e.*, percentage of cells with positive CI values) on different substrata as a function of PDGF-BB gradient. (d) Effect of Blebbistatin treatment on migration speed and CI of cells on fibers.

the substratum type (cell shape). We found that the spindle-shaped cells demonstrate a substantially higher chemotaxis sensitivity at shallower PDGF-BB concentration gradients and maintain a uniformly strong chemotaxis response across a wide range of PDGF-BB concentrations from 0-1 ng/mL to 0-10 ng/mL.

Conceptually, chemotaxis is comprised of three key components – motility, directional sensing, and polarity. The increased chemotaxis sensitivity of cells on fibers may be attributed to the marked differences in all three components. Cells on fibers with large spacing are on average 45% faster. Furthermore, due to the substrate geometry, cells on fibers have higher aspect ratios (390% higher AR value for spindle-shaped cells, compared to the cells in spread morphology) and are constrained in the gradient direction, both of which enhance the directional sensing and reduce lateral noise[59]. Lastly, the chemotaxis response relies on spatial sensing and is a function of the difference in the number of bound chemoreceptors between the front and the back of the cell. The significantly larger aspect ratio of cells on fibers (**Figure 2b**) presumably amplifies small gradients through sensing a larger difference in PDGF-BB concentration. Altogether, this results in the 3T3 cells in spindle morphology to exhibit the most sensitive chemotaxis response (highest CR) in concentration ranges as small as 0-1 ng/mL which is maintained up to 0-10 ng/mL range.

Pharmacological Inhibition of Mesenchymal Chemotaxis

We next wanted to investigate if the mesenchymal chemotaxis signaling pathway is conserved in cells on fibers, despite the significantly different chemotaxis response. Although the molecular circuits that control chemotaxis in mesenchymal cells are not as extensively explored as the amoeboid chemotaxis pathway, a recent study by S. Asokan *et al.* elegantly showed that regulation of non-muscle myosin IIA (MyoIIA), via its regulatory light chain serines 1 and 2 phosphorylation by a noncanonical PLCγ/PKCα pathway, is required for PDGF-BB chemotaxis[60]. The authors of this study showed that local inhibition of MyoIIA at the leading edge of the growth factor-stimulated chemotactic fibroblast and the resulting asymmetry in the MyoIIA concentration leads to increased contractility and retraction of the rear of the cell; thus pushing the cell in the direction of the leading edge. The same study also showed that inhibiting MyoIIA activity via BLB treatment blocks PDGF-BB based chemotaxis for fibroblasts on flat substrata.

Thus, the effect of BLB on 3T3 cell chemotaxis on the three substratum types at the optimal gradient of 0-10 ng/mL was investigated. Introduction of BLB blocked the PDGF-BB driven fibroblast chemotaxis and significantly reduced the CI of the cells which in turn reduced the CR value to approximately 50% (*i.e.*, no bias in the population migration, **Figure 5c-d**). However, no appreciable effect on the cell migration speed was observed (**Figure 5d**). Both observations are consistent with the results from S. Asokan *et al.* on flat substrata. The effect of BLB was reversible, *i.e.*, upon washing out the drug and reintroducing the PDGF-BB gradient, cells resumed their chemotaxis behavior (data not shown). These observations indicate that the main elements of the signaling pathway for mesenchymal chemotaxis on flat substrata is conserved for cells migrating on the suspended nanofibers.

Conclusions

A novel microfluidic assay device incorporated with ECM-mimicking nanofibers was developed to interrogate cell shape-driven plasticity in fibroblast chemotaxis response. By studying chemotaxis response to linear PDGF-BB concentration gradients on suspended polystyrene nanofibers, at small or large spacing, and flat polystyrene, significant differences in cell behavior on the different substrata were quantified. We document remarkable sensitivity in chemotaxis response to linear PDGF-BB concentration gradients in cells of different shapes on suspended nanofibers. Although the obligate pathway for mesenchymal chemotaxis towards the receptor tyrosine kinase (RTK) ligand PDGF-BB is conserved, cells on suspended fibers demonstrated substantially higher chemotaxis sensitivity and responded to an order of magnitude shallower PDGF-BB concentration gradient. Altogether, the strength of the chemotaxis response was dependent not only on the PDGF-BB gradient but also on the cell morphology (aspect ratio) which was modulated by varying the inter-fiber spacing. Given the heterogeneity in cell shape in physiologically relevant environments, the significant role of cell shape in mesenchymal chemotaxis response must be further explored. It is generally understood that a uniformly strong chemotaxis response to varying chemo-effector concentration gradients, as seen in **Figures 4d** and **5c** is a hallmark of amoeboid chemotaxis response (*e.g.*, neutrophils) and that PDGF-mediated chemotaxis response is less sensitive and strongly depends on the PDGF gradient and mid-point concentration[61]. Our findings, however, demonstrate that mesenchymal chemotaxis is strongly modulated by the cell shape and can be significantly different from the behavior observed on flat 2D substrata.

These findings highlight the importance of studying cell migration and chemotaxis in *vitro* environments that are more representative of the ECM that cells migrate upon *in vivo*. Using fiber networks capable of isolating individual protrusions longitudinal and transverse to cell migration direction[62] or measuring cell forces[63], our integrative microfluidic platform raises a number of intriguing opportunities to investigate potential changes in the contribution of other mechanisms that control protrusive activity; *e.g.*, adhesive signaling and crosstalk between PDGF and integrin-dependent signaling pathways[64,65]. In the future, this platform will be further developed to enable the study of the cell decision-making process in the presence of competing biophysical and biochemical cues to gain insight into directed cell migration in developmental, disease and repair biology.

Author Contributions

BB led the project administration, conceptualization, methodology development, investigation, data curation, formal analysis, and manuscript preparation. ASN equally contributed to the conceptualization, contributed to the investigation, and manuscript preparation. CMM contributed to data curation, formal analysis, investigation, methodology development, and manuscript preparation. AM contributed to data curation, formal analysis, and investigation. EJL and MAT contributed to the methodology development related to the microfluidic device. AK and EMS supported methodology development related to the microfluidic device.

Conflicts of interest

There are no conflicts to declare.

Acknowledgments

This project was partially supported by the National Science Foundation (CAREER award, CBET-1454226 to BB and CMMI-1437101 and CMMI-1462916 awarded to ASN, and REU-site DMR-0851662). CMM acknowledges financial support from the Robert E. Hord, Jr. Mechanical Engineering Graduate Fellowship.

References

1 S. Kurosaka and A. Kashina, *Birth Defects Res. Part C Embryo Today Rev.*, 2008, **84**, 102–122.
2 P. Martin, *Science*, 1997, **276**, 75–81.
3 T. Velnar, T. Bailey and V. Smrkolj, *J. Int. Med. Res.*, 2009, **37**, 1528–1542.
4 E. T. Roussos, J. S. Condeelis and A. Patsialou, *Nat. Rev. Cancer*, 2011, **11**, 573–587.
5 R. Kalluri and M. Zeisberg, *Nat. Rev. Cancer*, 2006, **6**, 392–401.
6 G. Parsonage, A. D. Filer, O. Haworth, G. B. Nash, G. E. Rainger, M. Salmon and C. D. Buckley, *Trends Immunol.*, 2005, **26**, 150–156.
7 P. P. Provenzano, K. W. Eliceiri, J. M. Campbell, D. R. Inman, J. G. White and P. J. Keely, *BMC Med.*, 2006, **4**, 38.
8 J. Franco-Barraza, R. Francescone, T. Luong, N. Shah, R. Madhani, G. Cukierman, E. Dulaimi, K. Devarajan, B. L. Egleston, E. Nicolas, R. Katherine Alpaugh, R. Malik, R. G. Uzzo, J. P. Hoffman, E. A. Golemis and E. Cukierman, *Elife*, 2017, **6**, e20600.
9 C. A. Parent, B. J. Blacklock, W. M. Froehlich, D. B. Murphy and P. N. Devreotes, *Cell*, 1998, **95**, 81–91.
10 S. Boyden, *J. Exp. Med.*, 1962, **115**, 453–466.
11 S. H. Zigmond, *J. Cell Biol.*, 1977, **75**, 606–616.
12 J. Adler, *Science*, 1966, **153**, 708–716.
13 Z. Pujic, D. Mortimer, J. Feldner and G. J. Goodhill, *Comb. Chem. High Throughput Screen.*, 2009, **12**, 580–588.
14 M. Ehrbar, a Sala, P. Lienemann, a Ranga, K. Mosiewicz, a Bittermann, S. C. Rizzi, F. E. Weber and M. P. Lutolf, *Biophys. J.*, 2011, **100**, 284–93.
15 C. Y. Chung, S. Funamoto and R. A. Firtel, *Trends Biochem. Sci.*, 2001, **26**, 557–566.
16 H. Cai and P. N. Devreotes, *Semin. Cell Dev. Biol.*, 2011, **22**, 834–841.
17 J. E. Bear and J. M. Haugh, *Curr. Opin. Cell Biol.*, 2014, **30**, 74–82.
18 W. J. Polacheck, R. Li, S. G. M. Uzel and R. D. Kamm, *Lab Chip*, 2013, **13**, 2252–2267.
19 J. Dou and J.-M. Lin, in *Cell Analysis on Microfluidics*, ed. J.-M. Lin, Springer, Singapore, Singapore, 2018, pp. 149–179.
20 A. D. Doyle, F. W. Wang, K. Matsumoto and K. M. Yamada, *J. Cell Biol.*, 2009, **184**, 481–90.
21 P. Keely and A. Nain, *F1000Research*, 2015, **4**.
22 R. Rangarajan and M. H. Zaman, *Cell Adh. Migr.*, 2008, **2**, 106–109.
23 U. Haessler, Y. Kalinin, M. A. Swartz and M. Wu, *Biomed. Microdevices*, 2009, **11**, 827–835.
24 G. Charras and E. Sahai, *Nat. Rev. Mol. Cell Biol.*, 2014, **15**, 813–824.
25 W.-C. Hung, S.-H. Chen, C. D. Paul, K. M. Stroka, Y.-C. Lo, J. T. Yang and K. Konstantopoulos, *J. Cell Biol.*, 2013, **202**, 807–824.
26 S. Meehan and A. S. Nain, *Biophys. J.*, 2014, **107**, 2604–11.
27 P. Wu, A. Giri, S. X. Sun and D. Wirtz, *Proc. Natl. Acad. Sci. U. S. A.*, 2014, **111**, 3949–3954.
28 R. J. Petrie, N. Gavara, R. S. Chadwick and K. M. Yamada, *J. Cell Biol.*, 2012, **197**, 439–455.
29 G. S. Jeong, G. H. Kwon, A. R. Kang, B. Y. Jung, Y. Park, S. Chung and S.-H. Lee, *Biomed. Microdevices*, 2011, **13**, 717–723.
30 V. V. Abhyankar, M. W. Toepke, C. L. Cortesio, M. A. Lokuta, A. Huttenlocher and D. J. Beebe, *Lab Chip*, 2008, **8**, 1507–1515.
31 D. I. Shreiber, P. A. J. Enever and R. T. Tranquillo, *Exp. Cell Res.*, 2001, **266**, 155–166.
32 K. Wolf, I. Mazo, H. Leung, K. Engelke, U. H. von Andrian, E. I. Deryugina, A. Y. Strongin, E.-B. Bröcker and P. Friedl, *J. Cell Biol.*, 2003, **160**, 267–277.
33 M. H. Zaman, L. M. Trapani, A. L. Sieminski, A. Siemeski, D. Mackellar, H. Gong, R. D. Kamm, A. Wells, D. A. Lauffenburger and P. Matsudaira, *Proc. Natl. Acad. Sci. U. S. A.*, 2006, **103**, 10889–94.
34 C. Guetta-Terrier, P. Monzo, J. Zhu, H. Long, L. Venkatraman, Y. Zhou, P. Wang, S. Y. Chew, A. Mogilner, B. Ladoux and N. C. Gauthier, *J. Cell Biol.*, 2015, **211**, 683–701.
35 H. G. Sundararaghavan, R. L. Saunders, D. A. Hammer and J. A. Burdick, *Biotechnol. Bioeng.*, 2013, **110**, 1249–1254.
36 P. Sharma, C. Ng, A. Jana, A. Padhi, P. Szymanski, J. S. H. Lee, B. Behkam and A. S. Nain, *Mol. Biol. Cell*, 2017, **28**, 2579–2588.
37 K. Sheets, S. Wunsch, C. Ng and A. S. Nain, *Acta Biomater.*, 2013, **9**, 7169–7177.
38 A. S. Nain Phillippi, J.A., Sitti, M., MacKrell, K., Campbell, P.G., Amon, C., A. S. Nain, J. a Phillippi, M. Sitti, J. Mackrell, P. G. Campbell and C. Amon, *Small*, 2008, **4**, 1153–1159.
39 H. Seppä, G. Grotendorst, S. Seppä, E. Schiffmann and G. R. Martin, *J. Cell Biol.*, 1982, **92**, 584–8.
40 A. Siegbahn, A. Hammacher, B. Westermark and C. H. Heldin, *J. Clin. Invest.*, 1990, **85**, 916–920.
41 A. S. Nain, M. Sitti, A. Jacobson, T. Kowalewski and C. Amon, *Macromol. Rapid Commun.*, 2009, **30**, 1406–1412.
42 A. S. Nain and J. Wang, *Polym. J.*, 2013, **45**, 1–6.
43 J. Wang and A. S. Nain, *Langmuir*, 2014, **30**, 13641–13649.
44 E. D. Hay, *Cell Biology of Extracellular Matrix*, Springer, New York, 1991.
45 P. P. Provenzano, D. R. Inman, K. W. Eliceiri, J. G. Knittel, L. Yan, C. T. Rueden, J. G. White and P. J. Keely, *BMC Med.*, 2008, **6**, 11.
46 M. P. E. Wenger, L. Bozec, M. A. Horton and P. Mesquida, *Biophys. J.*, 2007, **93**, 1255–63.
47 F. H. Silver, J. W. Freeman and G. P. Seehra, *J. Biomech.*, 2003, **36**, 1529–53.
48 S. van Helvert, C. Storm and P. Friedl, *Nat. Cell Biol.*, 2018, **20**, 8–20.
49 E. Cukierman, R. Pankov, D. R. Stevens and K. M. Yamada,

Science (80-.)., 2001, **294**, 1708–1712.

50 G. E. Novotny and C. Gnoth, *J. Anat.*, 1991, **177**, 195–207.

51 N. L. Jeon, S. K. W. Dertinger, D. T. Chiu, I. S. Choi, A. D. Stroock and G. M. Whitesides, *Langmuir*, 2000, **16**, 8311–8316.

52 B. Li, M. Liu and Q. Chen, *J. Micro/Nanolithography, MEMS, MOEMS*, 2005, **4**, 043008.

53 B. Klenkler, H. Sheardown and L. Jones, *Ocul. Surf.*, 2007, **5**, 228–39.

54 M. Vesaluoma, A. M. Teppo, C. Grönhagen-Riska and T. Tervo, *Curr. Eye Res.*, 1997, **16**, 825–31.

55 J. P. Singh, M. A. Chaikin and C. D. Stiles, *J. Cell Biol.*, 1982, **95**, 667–671.

56 J. M. Cassano, J. G. Kennedy, K. A. Ross, E. J. Fraser, M. B. Goodale and L. A. Fortier, *Knee Surgery, Sport. Traumatol. Arthrosc.*, 2018, **26**, 333–342.

57 D. Irimia and M. Toner, *Integr. Biol.*, 2009, **1**, 489–556.

58 G. R. Grotendorst, *Cell*, 1984, **36**, 279–285.

59 J. M. Haugh and I. C. Schneider, *Chem. Eng. Sci.*, 2006, **61**, 5603–5611.

60 S. B. Asokan, H. E. Johnson, A. Rahman, S. J. King, J. D. Rotty, I. P. Lebedeva, J. M. Haugh and J. E. Bear, *Dev. Cell*, 2014, **31**, 747–760.

61 I. C. Schneider and J. M. Haugh, *J. Cell Biol.*, 2005, **171**, 883–892.

62 B. Koons, P. Sharma, Z. Ye, A. Mukherjee, M. H. Lee, D. Wirtz, B. Behkam and A. S. Nain, *ACS Nano*, 2017, **11**.

63 K. Sheets, J. Wang, W. Zhao, R. Kapania and A. S. Nain, *Biophys. J.*, 2016, **111**, 197–207.

64 R. Aguilar-Cuenca and M. Vicente-Manzanares, *Dev. Cell*, 2014, **31**, 669–70.

65 J. Gailit and R. A. F. Clark, *J. Invest. Dermatol.*, 1996, **106**, 102–108.